Opto-Electronic Advances

ISSN 2096-4579 CN 51-1781/TN

Physics-data-driven intelligent optimization for large-aperture metalenses

Yingli Ha, Yu Luo, Mingbo Pu, Fei Zhang, Qiong He, Jinjin Jin, Mingfeng Xu, Yinghui Guo, Xiaogang Li, Xiong Li, Xiaoliang Ma and Xiangang Luo

Citation: Ha YL, Luo Y, Pu MB, Zhang F, He Q et al. Physics-data-driven intelligent optimization for large-aperture metalenses. *Opto-Electron Adv* **6**, 230133(2023).

https://doi.org/10.29026/oea.2023.230133

Received: 1 August 2023; Accepted: 9 October 2023; Published online: 15 November 2023

Opto-Electronic Advances

Article

November 2023, Vol. 6, No. 11

DOI: 10.29026/oea.2023.230133

Physics-data-driven intelligent optimization for large-aperture metalenses

Yingli Ha[1,2,3†], Yu Luo[1,2,3†], Mingbo Pu[1,2,3,4*], Fei Zhang[1,2,3], Qiong He[1,2], Jinjin Jin[1,2], Mingfeng Xu[1,2,3,4], Yinghui Guo[1,2,3,4], Xiaogang Li[5], Xiong Li[1,2,4], Xiaoliang Ma[1,2,4] and Xiangang Luo[1,2,3,4*]

Metalenses have gained significant attention and have been widely utilized in optical systems for focusing and imaging, owing to their lightweight, high-integration, and exceptional-flexibility capabilities. Traditional design methods neglect the coupling effect between adjacent meta-atoms, thus harming the practical performance of meta-devices. The existing physical/data-driven optimization algorithms can solve the above problems, but bring significant time costs or require a large number of data-sets. Here, we propose a physics-data-driven method employing an "intelligent optimizer" that enables us to adaptively modify the sizes of the meta-atom according to the sizes of its surrounding ones. The implementation of such a scheme effectively mitigates the undesired impact of local lattice coupling, and the proposed network model works well on thousands of data-sets with a validation loss of 3×10^{-3}. Based on the "intelligent optimizer", a 1-cm-diameter metalens is designed within 3 hours, and the experimental results show that the 1-mm-diameter metalens has a relative focusing efficiency of 93.4% (compared to the ideal focusing efficiency) and a Strehl ratio of 0.94. Compared to previous inverse design method, our method significantly boosts designing efficiency with five orders of magnitude reduction in time. More generally, it may set a new paradigm for devising large-aperture meta-devices.

Keywords: intelligence method; physics-data-driven method; inverse design; large-aperture metalenses

Ha YL, Luo Y, Pu MB, Zhang F, He Q et al. Physics-data-driven intelligent optimization for large-aperture metalenses. *Opto-Electron Adv* **6**, 230133 (2023).

Introduction

In the past decade, meta-devices have shown remarkable advantages of lightweight, high integration, and high flexibility capabilities[1–9], which have led to the emergence of many new types of flat optical components, including lenses[10,11], holograms[12–14], vector beam generator[2,15], and optical encryption[16,17]. Traditional design method of meta-devices is based on phase matching, which assigns a pre-defined phase profile to each meta-atom[18]. The method is based on the assumption of local phase approximation and each phase of the meta-atom is obtained using periodic boundary conditions. Therefore, for meta-devices with aperiodic layouts, the traditional design method neglects the local lattice

[1]National Key Laboratory of Optical Field Manipulation Science and Technology, Chinese Academy of Sciences, Chengdu 610209, China; [2]State Key Laboratory of Optical Technologies on Nano-Fabrication and Micro-Engineering, Institute of Optics and Electronics, Chinese Academy of Sciences, Chengdu 610209, China; [3]Research Center on Vector Optical Fields, Institute of Optics and Electronics, Chinese Academy of Sciences, Chengdu 610209, China; [4]School of Optoelectronics, University of Chinese Academy of Sciences, Beijing 100049, China; [5]Tianfu Xinglong Lake Laboratory, Chengdu 610299, China.

[†]These authors contributed equally to this work.

*Correspondence: MB Pu, E-mail:pmb@ioe.ac.cn; XG Luo, E-mail: lxg@ioe.ac.cn

Received: 1 August 2023; Accepted: 9 October 2023; Published online: 15 November 2023

coupling effect between adjacent meta-atoms, thus leading to errors between the real electric field distribution and the ideal one[19]. Optimization algorithms can be used to improve the efficiency of the meta-device, but it is still not possible to completely eliminate the error introduced by coupling effects through independent optimization of each pixel[20]. Therefore, it is necessary to consider the interaction of the entire device and optimize it as a whole to obtain high-performance meta-devices.

Inverse design methods could iteratively update the real vectorial electric field for each pixel, gradually approaching the ideal electric field distribution, and can effectively solve the problems of the traditional design method[21–24]. The design of metadevices has incorporated intelligent methods, yielding outstanding outcomes[25–27]. Based on physics-driven or data-driven optimization algorithms, abundant methods of inverse design techniques have been studied[28–32]. Among them, adjoint-based optimization has demonstrated success in realizing device functions, such as metalens[33–35], disordered metasurface[23], and deflector[36,37]. The global optimal solution could be achieved by searching a large number of initial structures[22,38]. However, the above physics-driven methods are usually used to optimize small-scale meta-devices, typically, <100λ[33]. Most recently, more researchers have focused on inverse design methods based on the deep learning (DL) network[39–44], and considerable results have been achieved[45–49], such as deflector[50,51], 3D vectorial holography[52], multi-function meta-device[53], and multi-band absorber[46]. In addition, researchers try to alleviate the burden of numerical calculations, and accelerate optimization, by using semi-supervised learning strategies[54], self-supervised learning strategies[55], data-driven evolutionary algorithms[56], and physics-driven DL methods[50,51,57]. However, further optimization of the inverse design is highly challenging for large-scale meta-devices with aperiodic meta-atoms. One current feasible design method for large-scale aperiodic meta-devices is based on adjoint simulation and Chebyshev interpolation. Although this method can improve the efficiency of the meta-device, it still takes several hours to optimize a device with a diameter of 1000λ. In addition, most effective data-driven methods (DL networks) rely heavily on vast amounts of data-sets (tens of thousands of data)[58], complex network models (dozens of layers)[59], and poor generalization capabilities[50,51,57].

In this study, we propose a physics-data-driven design method that integrates a multi-objective optimization algorithm with a DL approach. We have developed an "intelligent optimizer" that utilizes an end-to-end design framework to achieve optimized design of large-aperture metalenses. Compared with physics-driven or data-driven optimization methods, our method has the advantages of simple network models (16 layers of neurons), low data-set requirements (~5000 data-sets), and short optimization time (6 min and 45 s@1 mm^2, 2 h and 54 min@1 cm^2). The simulation results provide evidence that the proposed method is capable of effectively optimizing the polarization-multiplexed metalens. In principle, the size of the designed metalens can be as large as hundreds of millimeters. It is experimentally demonstrated that a 1-mm-diameter metalens with an F-number of 1 (*NA*=0.44) could achieve a relative focusing efficiency of 93.4% (compared to the ideal focusing efficiency). Specifically, the same network is also applicable to optimize metalenses with higher F-numbers. To illustrate the advantages of the proposed method, Table 1 is listed, which sums up the representative parameters of various literature. In Table 1, RGB means the working wavelengths (λ) are red (470 nm), green (532 nm), and blue (633 nm). Additionally, h represents the hours, min represents the minutes and s represents the seconds.

Design principle

Compared with previous DL networks that learn the performance of the full-device, the proposed network is based on an end-to-end design. As shown in Figure 1, the "intelligent optimizer" consists of two optimization methods: the physics-driven method (adjoint-based shape optimization, Adj method) and the data-driven method (DL method). The adjoint-based shape optimization is utilized to produce high-quality data-sets, while the DL method is employed to enhance the focusing efficiency of the large-aperture metalens. To describe the target of the optimization algorithm more intuitively, the catenary-shaped electric field lines between two adjacent meta-atoms are used to indicate the coupling efficiency between the two adjacent meta-atoms[63–65]. The inputs for the network are geometric parameters of a super meta-atom (composed of adjacent $N \times N$ meta-atoms) which are sliced from the initial metalens in a specific order. The outputs are geometric parameters of one meta-atom which is sliced from the optimized metalens. The new metalens can be obtained by splicing the optimized meta-atoms in a consistent sequence. As a result, the new metalens has a significantly higher focusing efficiency

Table 1 | Examples to show the representative parameters and performance of various methods.

Ref.	λ (nm)	Material	NA	D (μm)	Dimension	Efficiency	Method	Time
Liang et al.[20]	532	TiO_2	0.98	-	2D	67%[a),e)]	Hybrid optimization algorithm	-
Cai et al.[29]	532	TiO_2	0.51	24	1D	60%[a),e)]	Genetic algorithm	1000 s
Mansouree et al.[33]	850	a-Si	0.78	52	2D	65%[a),e)]	Adjoint optimization	97 min/iteration
Li et al.[35]	RGB	TiO_2	0.3	10000	2D	15%[a),e)]	Conservative convex separable approximation	few hours
An et al.[41]	1550	p-Si	0.72	32	1D	77.62%[b),d)]	Deep learning	200 s
Phan et al.[60]	640	SOI	0.5	200	1D	89%[c),e)]	Topology optimization	100 h
Pestourie et al.[61]	RGB	TiO_2	0.3	235	1D	-	"Locally periodic" approximation	250 s
Arbabi et al.[62]	1550	a-Si	0.37	50	2D	82%[a),e)]	High-contrast gratings	-
This work	**1550**	**SOS**	**0.44**	**50.5**	**2*D***	**95.7%[c),d)]**	**Physics-data-driven method**	**15 s**
This work	**1550**	**SOS**	**0.44**	**1000**	**2*D***	**93.4%[c),e)]**	**Physics-data-driven method**	**6 min and 45 s**
This work	**1550**	**SOS**	**0.44**	**10000**	**2*D***	**~95%[c),f)]**	**Physics-data-driven method**	**2 h and 54 min**

[a)]Absolute focusing efficiency; [b)]Relative focusing efficiency; [c)]Relative focusing efficiency compared to the ideal efficiency; [d)]Simulated result; [e)]Experimental result; [f)]Predict result

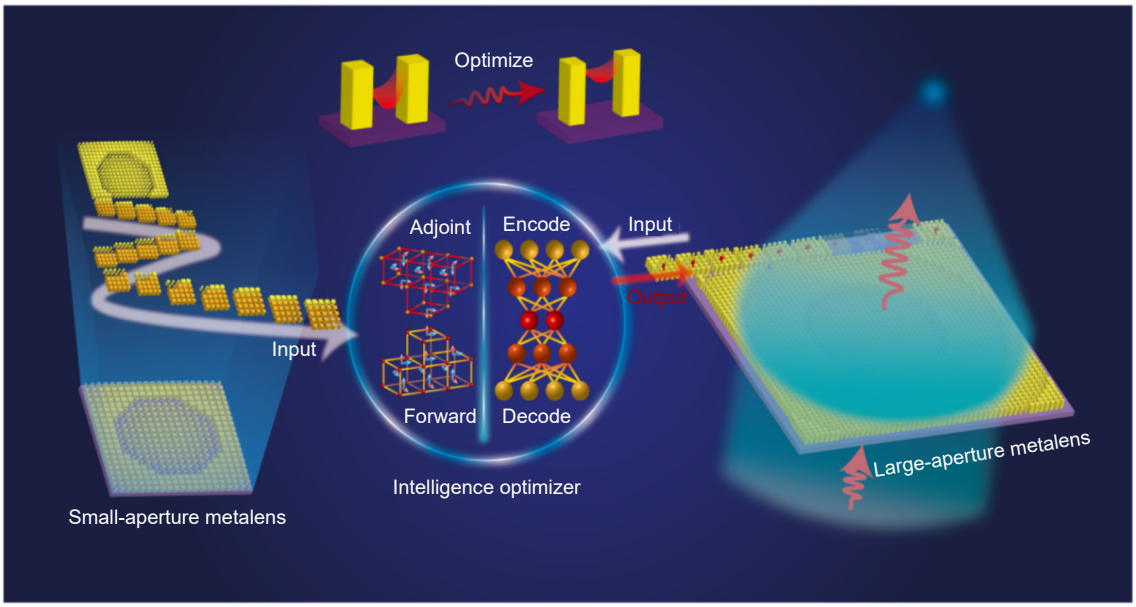

Fig. 1 | Working principle of the "intelligent optimizer". The "intelligent optimizer" incorporates both Adj and DL methods. Data-sets of the DL network are obtained from the small-aperture metalens optimized by the Adj method. Super meta-atoms of large-aperture metalens are fed into the network one by one. Output meta-atoms are spliced together to create a new metalens with improved focusing efficiency.

than the initial one.

High-quality data-sets can provide sufficient and accurate information to the network, allowing it to capture features better, improve its generalization ability, and increase validation accuracy. Therefore, choosing appropriate and high-quality data-sets is an indispensable step for training DL networks. Here, metalenses are artificially used as the basis of data-sets, which will be helpful in constructing high-quality data-sets. Essentially, the optimization of the metalens is to make the real phase distribution closer to the ideal one which can be obtained by Eq. (1). Therefore, coupling effects among random phase arrangement structures are neglected in this study. This strategy has contributed to reducing the amount of data-set requirements and the complexity of the model and allows the network to converge faster. Furthermore, to endow our network with optimization capabilities, we will use initial and optimized metalenses as inputs and outputs. The optimization algorithm is the Adj method and more details pertaining to the Adj method are provided in Supplementary information, Section 1.

To reduce the computational time and memory requirements associated with numerous simulation iterations, metalenses with the diameters of 30.5 μm and 40.5 μm are used in our dataset, and the mesh size for the

electric field simulation at 50 nm. The optimization of the small-aperture metalens can be separated into three steps. First, the initial meta-atoms for the initial metalens are selected. Eight kinds of meta-atoms cover the phase range 0-to-2π by replacing the ideal phase distribution with an approximated step-function. To maintain high transmission efficiency, the period and height of meta-atoms are set as 500 nm and 1000 nm, respectively. It is important to note that the period and height of the metalens optimized by the DL method should be consistent with the small-aperture metalens. Second, initial metalenses are designed. We designed polarization-multiplexed metalenses that can independently control *x*- and *y*- polarized light. The F-numbers of the above metalenses are both 1, and the focus spots for *x*-polarized incident light and *y*-polarized incident light are at the center of the focal plane. Therefore, the modulation of *x*- and *y*-polarization is identical for each initial metalens, leading to the same width and length for each meta-atom. The width/length of each meta-atom for the initial metalens is determined according to the phase profile given by Eq. (1).

$$\varphi = \frac{2\pi}{\lambda}\left(f - \sqrt{f^2 + (x - x_0)^2 + (y - y_0)^2}\right), \quad (1)$$

where f is the focal length, λ is the working wavelength, and x and y are the spatial positions on the lens. x_0 and y_0 correspond to the displacement of the focal spot from the center of the metalens. There is a one-to-one mapping between each phase and the size of the meta-atom, and the phase accuracy depends on the kinds of meta-atoms. At last, the Adj method is used to optimize the real electric field distribution. Although the Adj method is also useful for random distribution structures, it will enforce the one-to-one mapping to become many-to-one, bringing greater challenges for the network training. Taking the metalens with a diameter of 40.5 μm (81×81 meta-atoms) as an example, after 20 optimization iterations, all the meta-atoms sizes have been effectively corrected. As shown in Fig. 2(a), there is a difference of ±40 nm in widths between initial and optimized meta-atoms. Finally, metalenses have Strehl ratios of 0.96/0.958 and 0.95/0.945 for *x*/*y*-polarized light. The figure of merit (FoM) is desired transmitted field distribution which also indicates the Strehl ratio of the metalens.

Next, metalenses before and after optimization are used to build data-sets, that is, to carry out data pre-processing steps which can be separated into two steps. Firstly, the initial metalenses are divided into many super meta-atoms whose widths/lengths ultimately become the input data-sets. Considering that a coupling effect occurs within the distance range between a meta-atom and its surrounding two layers of meta-atoms, the size of a super meta-atom is 5×5 with a sliced interval of 1, and the output starting sampling position are located at the third row and third column of the sampled metalens. This means the design-loop will work on a 5×5 array with overlap. Since the initial metalens is isotropic, the input data-sets can only consist of widths or lengths. Secondly, the output data-sets are derived from the optimized metalens. One output data-set is 1×2 vector data consisting of the width and length of one meta-atom, which is the modified meta-atom positioned at the center of the super meta-atoms. Because the FoM of Adj method is based on both *x*- and *y*- polarized incident light, it makes the meta-atom eventually anisotropic, leading to the different width and length. The initial widths/lengths distribution of a metalens is shown in Fig. 2(b). There are two types of super meta-atoms, namely continuous change (smooth) box Ⅰ and discontinuous change (rough) box Ⅱ. The features of a smooth region are that the widths/lengths of the meta-atoms in the same region are increased, decreased, or remain unchanged along any direction. On the contrary, regions, where the widths/lengths change do not follow the above three patterns are referred to as rough regions. As a result, the metalens is divided into many super meta-atoms. Finally, we have 9178 data-sets consisting of two metalenses, of which 3960 data-sets belong to smooth regions and 5218 belong to the rough region. In the following, the validation loss of the network will prove that thousands of data-sets are enough for our network. Figure 2(c) shows the framework of the optimized network, which consists of an AutoEncoder network (A-network) and an inverse design network (I-network). The input data-sets are encoded and decoded, with the output data of the A-network being equal to the input data, promoting information depth mining. The latent layer carries all the information of the original input data in a different form, and the outputs of the A-network are coupled to the I-network which is utilized to generate the optimized meta-atoms.

Results and discussion

Two networks were trained for dealing with smooth and rough regions of data-sets. The architectures of

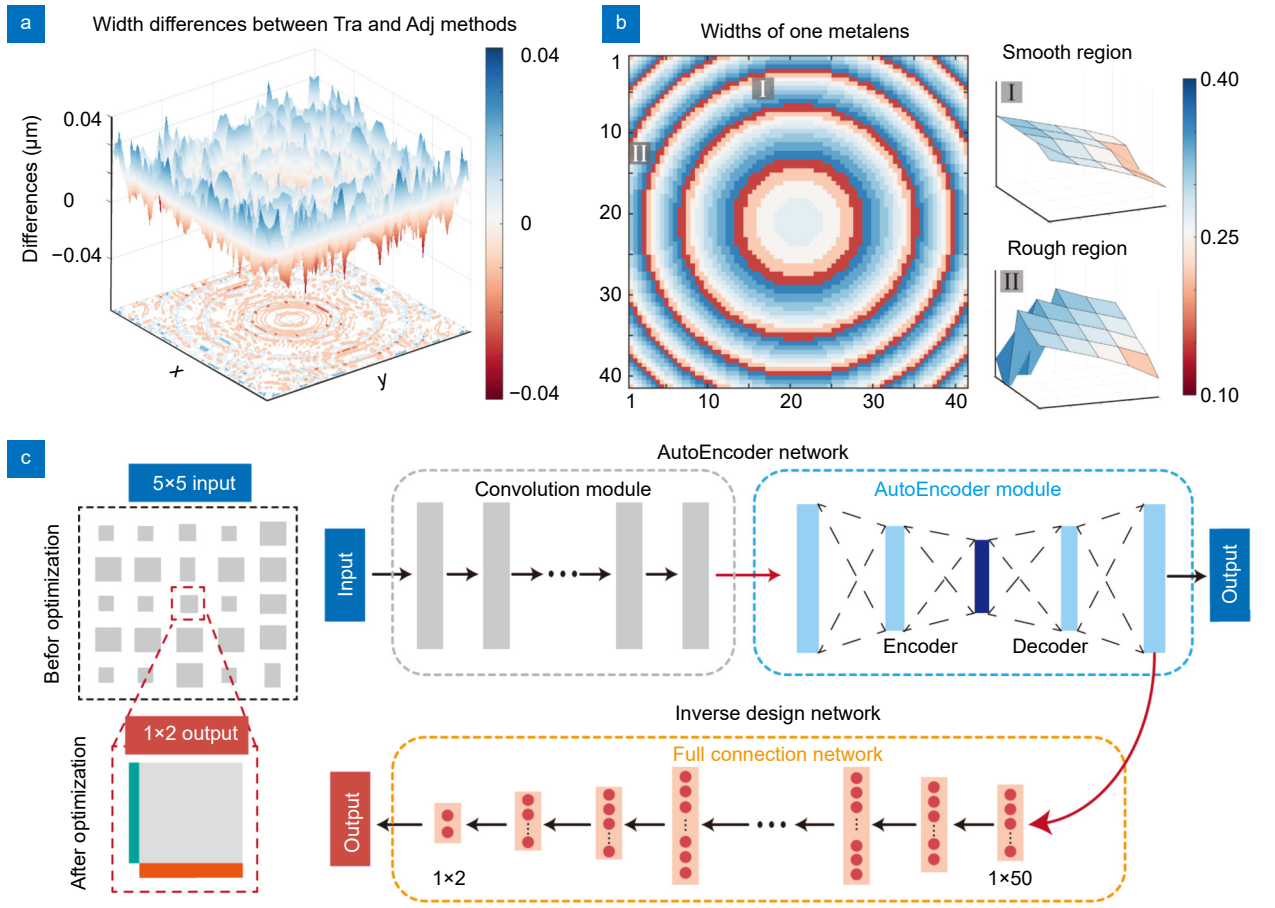

Fig. 2 | Design method for the large-aperture metalens. (**a**) The differences in widths distribution for the meta-atoms before and after optimization. (**b**) The widths distribution of metalens, with the smooth region and rough region corresponding to translucent boxes I and II, respectively. (**c**) The optimized network framework consists of an A-network that expands the information space of sampled data, and the weak coupling strength structures are filtered by the I-network.

A-network and I-network are shown in Supplementary information (see Section 2). The mean-absolute-error (MAE) loss function is used to measure the difference between the predicted values and the real values, and helps the optimizer adjust the model parameters to improve the prediction accuracy. After 5000 iterations, the MAEs for smooth and rough region networks are 3×10^{-3} and 2×10^{-3} (see Supplementary information, Section 3), corresponding to output errors of 3 nm and 2 nm (both within the fabrication error), respectively. The adopted network architecture, encompassing both the AutoEncoder network and the inverse design network, holds advantages over directly employing fullly connected neural (FCN) to obtain output. Because the adopted network architecture can encode input data into lower dimensional hidden representations, it establishes a more matching relationship between the input and output data, making it easier for the neural network to learn important features in the input data. The loss of the FCN is 7×10^{-3} which is greater than the loss of our network. The details of the FCN network and its performance are shown in Supplementary information (see Section 4).

The same as the design of the initial small-aperture metalens, the large-aperture metalens could also be designed by the same eight kinds of meta-atoms. To improve the focusing efficiency of large-aperture metalens, it will be sliced into many super meta-atoms, each consisting of 5×5 meta-atoms, and the input data to the network are widths/lengths of a super meta-atom. Using the trained DL network, we get many new output data-sets, each of which consists of the lengths and widths of the new meta-atom. Finally, the output data-sets can be arranged on the same path as the input slice path to form a new metalens. To verify the performance of the metalens optimized by the Adj method and our method, we optimized the same linear polarization-multiplexed metalens with a diameter of 50.5 μm using the aforementioned methods. The electric field distribution of the

designed metalenses can be obtained through Finite Difference Time Domain (FDTD) Solution software and the vector diffraction theory. The full-wave simulation results proved that the focusing efficiencies of both metalenses mentioned above are higher than the initial metalens at the working wavelength of 1550 nm.

Figure 3(a) and 3(b) shows electric field distributions and the intensity profiles for different metalens on the *xy* focal plane and *xz* plane. After 15 days of 20 optimization iterations, the relative and absolute focusing efficiencies of the metalens have been improved to 87%/86.8% and 78%/77.9% with the Adj method for *x*- and *y*-polarization, respectively. The final relative and absolute focusing efficiencies of the metalens designed with the proposed method are 86.5%/87.1% and 76%/76.6% for *x*- and *y*-polarized light, and the optimization time is within 15 s. Here, the absolute focusing efficiency is defined as the ratio between the light intensity from the focal spot and the incident intensity, which can also be calculated by the product of transmission efficiency and the relative efficiency of the device. The relative focusing efficiency is defined as the ratio between the light intensity from the focal spot and the focal plane. The Strehl ratios of *x*- and *y*-polarized light are 0.95/0.957 and 0.96/0.96 for the metalenses designed by the DL method and Adj method, respectively. Figure 3(c, d) show the widths distribution on the y=0 plane (x>0) designed by three methods and compare them with the initial structure distribution on the y=0 plane (x>0). As shown in Fig. 3(d), there is a difference between the width obtained by the above two methods and the width obtained by the traditional method. Although the width changes in each pixel are inconsistent, the metalenses formed by them all exhibit high focusing efficiencies, which may result from non-convex optimization. The above simulation results have proved that the method

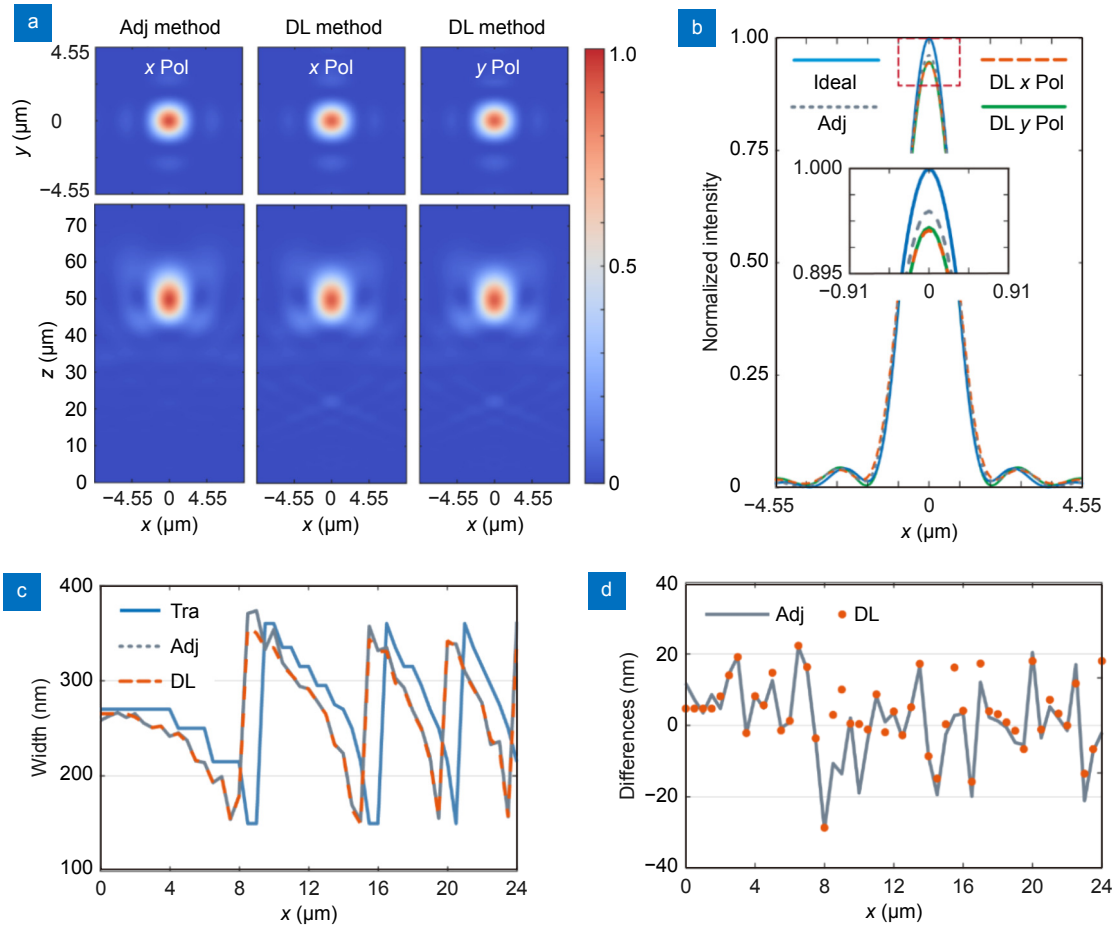

Fig. 3 | Simulation results of Adj and DL methods. (**a**) Electric field distributions in the *xy* and *xz* planes designed by DL method for *x*- and *y*-polarized light, and the Adj method for *x*-polarized, respectively. (**b**) Electric intensity profiles of the focal spot designed by theory, Adj, and DL methods, respectively. (**c**) Width distributions of metalenses on y=0 plane (x>0) designed by the traditional (Tra), Adj, and the proposed methods, respectively. (**d**) Width differences between the initial metalens and the optimized metalenses designed by the Adj method and our methods.

base on the DL network can achieve vector optimization for large-aperture metalens while significantly reducing the required time by five orders of magnitude.

To verify the optimization capability of the network for larger-aperture metalenses, two metalenses with diameters of 60.5 μm and 100.5 μm were optimized, respectively. The electric field distributions are shown in Supplementary information Section 4 (see Fig. S6), and the metalenses have the efficiencies and Strehl ratios of 86.6%, 86.2%, 0.97, and 0.96, respectively. In summary, the simulated focusing efficiency of metalenses with NA of 0.44, varying in diameter, consistently exceeds 86%. It can be inferred that the relative focusing efficiency of metalenses with NA of 0.44 optimized by DL method is about 95% (compared to the ideal focusing efficiency). Furthermore, to validate the generalization ability of the network, three metalenses with NAs of 0.3, 0.35, and 0.4 were optimized, and the corresponding electric field distributions are shown in Supplementary information Section 5 (see Fig. S7). The above metalenses have efficiencies and Strehl ratios of 86.4%, 86.6%, 87.7%, 0.94, 0.95, and 0.95, respectively. The above results have demonstrated that the trained network can optimize large-aperture metasurfaces with F-numbers ≥ 1 when the data-sets consists of metalens with an F-number of 1.

For further proof of concept, the optimized metalenses with diameters of 100.5 μm, 500 μm, and 1 mm with F-numbers of 1 were fabricated using the electron beam lithography technology on the silicon-on-sapphire substrate. Figure 4(a) shows the optical microscope and the scanning electron microscope (SEM) images of the fabricated metalenses, where the relative efficiencies of the metalenses under the illumination of the linear polarized laser beam are measured. Considering the photoelectric response of the CCD to the incident laser energy shows certain nonlinear response characteristics[66], a power meter is used to detect the relative efficiency (see Fig. S10, Supplementary information for experiment set-up). A focusing lens and a precision pinhole are used to constrain the size of the incident light and focused spot, respectively. Lens modulation ensures that the beam size of the incident light is smaller than that of the metalens. Additionally, a precision pinhole is placed behind the metalens to filter out power outside the focus range.

The fabricated metalenses all have an NA of 0.44, and the ideal FWHMs of the metalenses are ~1.57 μm, calculated by the vectorial angle spectrum method. The diameter of the precision pinhole is 10±1 μm, matching the size of the effective focal spot (a circular region centered on the peak intensity with a radius of treble FWHMs, and the diameter is 9.42 μm). The power meter is placed behind the precision pinhole to measure the focusing power and the focal plane power will be measured when the precision pinhole is removed. Considering the short focal length of a metalens with a diameter of 100.5 μm, an objective lens with 100× magnification is used to pair with a tube lens to magnify the image of the focal spot. An aperture with diameter of 1 mm is chosen to replace the precision pinhole, and other processes are the same as above. Under the illumination of a 1550 nm laser, the relative focusing efficiency of the DL-optimized metalens with a diameter of 1 mm is 85%, which is 93.4% of the ideal relative focusing efficiency. Furthermore, Fig. 4(d) shows the relative focusing efficiencies (compare to the ideal focusing efficiency) and Strehl ratios of the three metalenses.

Furthermore, the distribution of the focal spot on *xy* and *xz* planes is shown in Fig. 4(b, c). Figure 4(b) shows the normalized focusing intensity along the optical axis of the ideal metalens and the DL-optimized metalens, where the sub-maximum intensity of the ideal focal spot is used to normalize the intensity of the DL-optimized focal spot and the ideal focal spot. The Strehl ratio is defined as the ratio of the maximum intensity of the DL-optimized focal spot and the ideal focal spot. Objectives with large *NA*=0.7 are used to avoid the limited field of view of transmitted light. The experimental set-up is shown in Fig. S12 (Supplementary information). The imaging performance of the metalens (with a diameter of ~1 mm) is further characterized by the USAF 1951 resolution test chart (see Fig. S13, Supplementary information for experiment set-up), as shown in Fig. 4(e). The imaging result is obtained from group 7, where the smallest feature size is 2.19 μm of element No.6, and it can be clearly resolved. As a comparison, the imaging result of the ideal metalens (with a diameter of ~1 mm) is demonstrated, which is obtained through the convolution of ideal metalens focusing spot and resolution test chart. Experimental results show that the electromagnetic properties of metalenses designed by our DL method are close to those of ideal metalenses.

Conclusions

In this work, an "intelligent optimizer" is proposed to solve the challenges associated with efficiently optimizing large-aperture 2D metalens. The simulated and

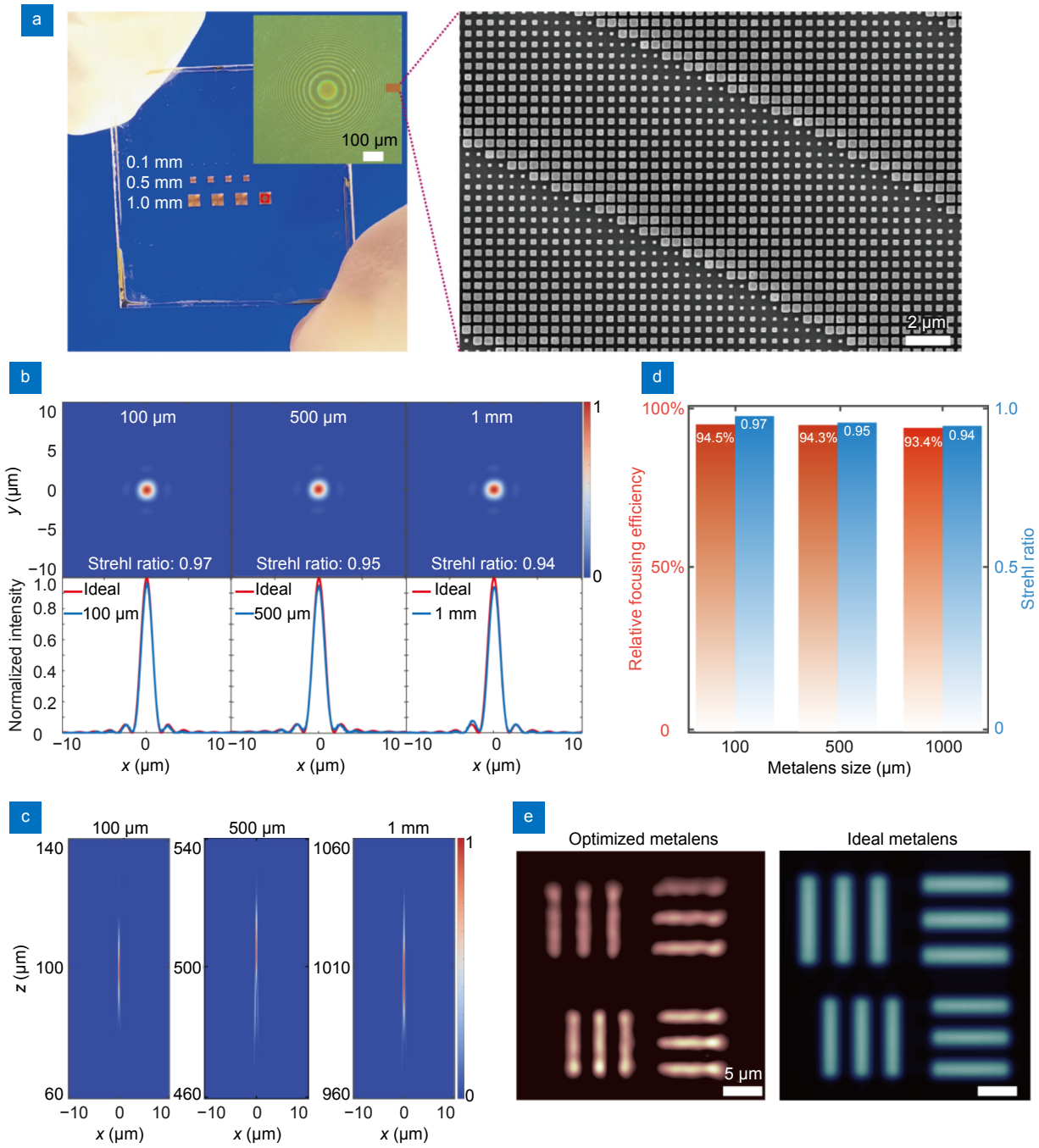

Fig. 4 | Experimental results of optimized metalenses. (**a**) The left image shows an overview of the device, with each diameter corresponding to four exposure doses. The inset is the optical microscope image. Scale bar: 100 μm. The right image is the scanning electron microscope image. Scale bar: 2 μm. (**b**) The first row shows the focal plane intensity distributions of the three metalenses (100.5 μm, 500 μm, and 1 mm, from left to right, respectively). The second row shows the normalized focal intensity along the *x*-axis at the focal plane of the three metalenses. (**c**) Focal intensity distributions in the *xz* plane at the three metalenses. (**d**) Relative focusing efficiencies and Strehl ratios of three metalenses. (**e**) Imaging results of elements #5 and #6 from group #7 of the USAF resolution target at 1 mm diameter optimized metalens (left) and 1 mm diameter ideal metalens (right). Scale bar: 5 μm.

experimental results demonstrate the significant potential of this optimizer in developing high-efficiency metalens technology. By leveraging the geometry parameters information from a high-performance metalens with a μm-scale diameter, we successfully optimize the geometry parameters of a cm-scale metalens. The optimized metalens, with a diameter of 1 mm consisting of 4×10^6 meta-atoms, can be optimized only in 6 min and 45 s. It has a relative focusing efficiency of 93.4% (compared to ideal focusing efficiency) and a Strehl ratio of

0.94. Furthermore, as aforementioned, the optimizer has the ability to scale downwards. Each size of meta-atoms in the metalens represents a phase, which means that optimizing the size of a meta-atom is also an optimization of the phase. By adding incident wavelength information to the network or increasing the number of input structures, we can optimize the more complex structural functional devices, as our proposed method essentially suppresses coupling effects and does not target a specific functional device. The proposed optimization is not limited to polarization-multiplexed metalenses, and it can also be used for other meta-devices, such as achromatic metalenses, wide-angle metalenses, orbital angular momentum metalenses, meta-holograms, etc.

Methods

The full-wave simulations of the metalenses were performed with FDTD Solutions. Both *x*- and *y*-polarized plane waves were normally incident from the bottom of the metalenses in the +*z* direction, with the boundary conditions are set as the perfectly matched layer along *x*, *y*, and *z* directions. The working wavelength was 1550 nm, and the mesh size was 50 nm. The data-sets were established using the FDTD solver, and it took ~15 days to complete 20 iterations of optimization. The DL network was trained using Tensorflow and the training time was about 40 minutes. The optimization time for metalenses with diameters of 100.5 μm, 500 μm, 1000 μm, and 10000 μm are 20 s, 2 min and 45 s, 6 min and 45 s, and 2 h and 54 min, respectively. Except from the simulation of the electric field, all the computation is dealt with the Pycharm software on an Intel Xeon Gold 6254 CPU Processor with a base clock of 3.09 GHz, 128 GB of RAM. The metasurfaces were fabricated by electron beam lithography techniques. The fabrication flow chart and the SEM images of the metalens with a diameter of 1 mm are shown in Supplementary information Figs. S8 and S9. The electric field and the imaging results of the metalens were characterized by the setup (see Supplementary information Figs. S10, S12, and S13 for detailed description).

References

1. Ren HR, Briere G, Fang XY, Ni PN, Sawant R et al. Metasurface orbital angular momentum holography. *Nat Commun* **10**, 2986 (2019).
2. Zhang YX, Pu MB, Jin JJ, Lu XJ, Guo YH et al. Crosstalk-free achromatic full Stokes imaging polarimetry metasurface enabled by polarization-dependent phase optimization. *Opto-Electron Adv* **5**, 220058 (2022).
3. Fu R, Chen KX, Li ZL, Yu SH, Zheng GX. Metasurface-based nanoprinting: principle, design and advances. *Opto-Electron Sci* **1**, 220011 (2022).
4. Zhang XD, Liu YL, Han JC, Kivshar Y, Song QH. Chiral emission from resonant metasurfaces. *Science* **377**, 1215–1218 (2022).
5. Zhou JX, Liu SK, Qian HL, Li YH, Luo HL et al. Metasurface enabled quantum edge detection. *Sci Adv* **6**, eabc4385 (2020).
6. Luo XG, Zhang F, Pu MB, Xu MF. Catenary optics: a perspective of applications and challenges. *J Phys:Condens Matter* **34**, 381501 (2022).
7. Xie X, Pu MB, Jin JJ, Xu MF, Guo YH et al. Generalized pancharatnam-berry phase in rotationally symmetric meta-atoms. *Phys Rev Lett* **126**, 183902 (2021).
8. Shen Y, Luo XG. Efficient bending and focusing of light beam with all-dielectric subwavelength structures. *Opt Commun* **366**, 174–178 (2016).
9. Wang YL, Fan QB, Xu T. Design of high efficiency achromatic metalens with large operation bandwidth using bilayer architecture. *Opto-Electron Adv* **4**, 200008 (2021).
10. Ogawa C, Nakamura S, Aso T, Ikezawa S, Iwami K. Rotational varifocal moiré metalens made of single-crystal silicon meta-atoms for visible wavelengths. *Nanophotonics* **11**, 1941–1948 (2022).
11. Zhang F, Pu MB, Li X, Ma XL, Guo YH et al. Extreme - angle silicon infrared optics enabled by streamlined surfaces. *Adv Mater* **33**, 2008157 (2021).
12. Georgi P, Wei QS, Sain B, Schlickriede C, Wang YT et al. Optical secret sharing with cascaded metasurface holography. *Sci Adv* **7**, eabf9718 (2021).
13. Khaliq HS, Kim J, Naeem T, Riaz K, Badloe T et al. Broadband chiro - optical effects for futuristic meta - holographic displays. *Adv Opt Mater* **10**, 2201175 (2022).
14. Gao H, Fan XH, Xiong W, Hong MH. Recent advances in optical dynamic meta-holography. *Opto-Electron Adv* **4**, 210030 (2021).
15. Jin JJ, Pu MB, Wang YQ, Li X, Ma XL et al. Multi-channel vortex beam generation by simultaneous amplitude and phase modulation with two-dimensional metamaterial. *Adv Mater Technol* **2**, 1600201 (2017).
16. Fang XY, Ren HR, Gu M. Orbital angular momentum holography for high-security encryption. *Nat Photonics* **14**, 102–108 (2020).
17. Zhang F, Guo YH, Pu MB, Chen LW, Xu MF et al. Meta-optics empowered vector visual cryptography for high security and rapid decryption. *Nat Commun* **14**, 1946 (2023).
18. Yu NF, Genevet P, Kats MA, Aieta F, Tetienne JP et al. Light propagation with phase discontinuities: generalized laws of reflection and refraction. *Science* **334**, 333–337 (2011).
19. Wang SM, Wu PC, Su VC, Lai YC, Hung Chu C et al. Broadband achromatic optical metasurface devices. *Nat Commun* **8**, 187 (2017).
20. Liang HW, Lin QL, Xie XS, Sun Q, Wang Y et al. Ultrahigh numerical aperture metalens at visible wavelengths. *Nano Lett* **18**, 4460–4466 (2018).
21. Ha YL, Guo YH, Pu MB, Xu MF, Li X et al. Meta-optics-empowered switchable integrated mode converter based on the adjoint method. *Nanomaterials* **12**, 3395 (2022).
22. Pan MY, Fu YF, Zheng MJ, Chen H, Zang YJ et al. Dielectric

metalens for miniaturized imaging systems: progress and challenges. *Light Sci Appl* **11**, 195 (2022).
23. Xu MF, He Q, Pu MB, Zhang F, Li L et al. Emerging long‐range order from a freeform disordered metasurface. *Adv Mater* **34**, 2108709 (2022).
24. Qi HX, Du ZC, Hu XY, Yang JY, Chu SS et al. High performance integrated photonic circuit based on inverse design method. *Opto-Electron Adv* **5**, 210061 (2022).
25. Liu XY, Chen MK, Chu CH, Zhang JC, Leng BR et al. Underwater binocular meta-lens. *ACS Photonics* **10**, 2382–2389 (2023).
26. Chen MK, Liu XY, Wu YF, Zhang JC, Yuan JQ et al. A metadevice for intelligent depth perception. *Adv Mater* **35**, 2107465 (2023).
27. Chen MK, Liu XY, Sun YN, Tsai DP. Artificial intelligence in meta-optics. *Chem. Rev* **122**, 15356–15413 (2022).
28. Dory C, Vercruysse D, Yang KY, Sapra NV, Rugar AE et al. Inverse-designed diamond photonics. *Nat Commun* **10**, 3309 (2019).
29. Cai HG, Srinivasan S, Czaplewski DA, Martinson ABF, Gosztola DJ et al. Inverse design of metasurfaces with non-local interactions. *npj Comput Mater* **6**, 116 (2020).
30. Chung H, Miller OD. High-NA achromatic metalenses by inverse design. *Opt Express* **28**, 6945–6965 (2020).
31. Lalau-Keraly CM, Bhargava S, Miller OD, Yablonovitch E. Adjoint shape optimization applied to electromagnetic design. *Opt Express* **21**, 21693–21701 (2013).
32. Nam SH, Kim M, Kim N, Cho D, Choi M et al. Photolithographic realization of target nanostructures in 3D space by inverse design of phase modulation. *Sci Adv* **8**, eabm6310 (2022).
33. Mansouree M, McClung A, Samudrala S, Arbabi A. Large-scale parametrized metasurface design using adjoint optimization. *ACS Photonics* **8**, 455–463 (2021).
34. Sang D, Xu MF, Pu MB, Zhang F, Guo YH et al. Toward high-efficiency ultrahigh numerical aperture freeform metalens: from vector diffraction theory to topology optimization. *Laser Photonics Rev* **16**, 2200265 (2022).
35. Li ZY, Pestourie R, Park JS, Huang YW, Johnson SG et al. Inverse design enables large-scale high-performance meta-optics reshaping virtual reality. *Nat Commun* **13**, 2409 (2022).
36. Sell D, Yang JJ, Doshay S, Yang R, Fan JA. Large-angle, multifunctional metagratings based on freeform multimode geometries. *Nano Lett* **17**, 3752–3757 (2017).
37. Xu MF, Pu MB, Sang D, Zheng YH, Li X et al. Topology-optimized catenary-like metasurface for wide-angle and high-efficiency deflection: from a discrete to continuous geometric phase. *Opt Express* **29**, 10181–10191 (2021).
38. Yang JJ, Fan JA. Topology-optimized metasurfaces: impact of initial geometric layout. *Opt Lett* **42**, 3161–3164 (2017).
39. Ma TG, Tobah M, Wang HZ, Guo LJ. Benchmarking deep learning-based models on nanophotonic inverse design problems. *Opto-Electron Sci* **1**, 210012 (2022).
40. Zhelyeznyakov MV, Brunton SL, Majumdar A. Deep learning to accelerate Maxwell's equations for inverse design of dielectric metasurfaces. In *Proceedings of 2021 Conference on Lasers and Electro-Optics* 1–2 (IEEE, 2020).
41. An SS, Zheng BW, Shalaginov MY, Tang H, Li H et al. Deep convolutional neural networks to predict mutual coupling effects in metasurfaces. *Adv Opt Mater* **10**, 2102113 (2022).
42. Lin Z, Roques-Carmes C, Pestourie R, Soljačić M, Majumdar A et al. End-to-end nanophotonic inverse design for imaging and polarimetry. *Nanophotonics* **10**, 1177–1187 (2021).
43. Yeung C, Tsai JM, King B, Pham B, Ho D et al. Multiplexed supercell metasurface design and optimization with tandem residual networks. *Nanophotonics* **10**, 1133–1143 (2021).
44. Krasikov S, Tranter A, Bogdanov A, Kivshar Y. Intelligent metaphotonics empowered by machine learning. *Opto-Electron Adv* **5**, 210147 (2022).
45. Ma W, Liu ZC, Kudyshev ZA, Boltasseva A, Cai WS et al. Deep learning for the design of photonic structures. *Nat Photonics* **15**, 77–90 (2021).
46. Qiu TS, Shi X, Wang JF, Li YF, Qu SB et al. Deep learning: a rapid and efficient route to automatic metasurface design. *Adv Sci* **6**, 1900128 (2019).
47. Jiang JQ, Chen MK, Fan JA. Deep neural networks for the evaluation and design of photonic devices. *Nat Rev Mater* **6**, 679–700 (2021).
48. Qian C, Zheng B, Shen YC, Jing L, Li EP et al. Deep-learning-enabled self-adaptive microwave cloak without human intervention. *Nat Photonics* **14**, 383–390 (2020).
49. Yang B, Ma DN, Liu WW, Choi DY, Li ZC et al. Deep-learning-based colorimetric polarization-angle detection with metasurfaces. *Optica* **9**, 217–220 (2022).
50. Jiang JQ, Fan JA. Global optimization of dielectric metasurfaces using a physics-driven neural network. *Nano Lett* **19**, 5366–5372 (2019).
51. Jiang JQ, Sell D, Hoyer S, Hickey J, Yang JJ et al. Free-form diffractive metagrating design based on generative adversarial networks. *ACS Nano* **13**, 8872–8878 (2019).
52. Ren HR, Shao W, Li Y, Salim F, Gu M. Three-dimensional vectorial holography based on machine learning inverse design. *Sci Adv* **6**, eaaz4261 (2020).
53. Ma W, Xu YH, Xiong B, Deng L, Peng RW et al. Pushing the limits of functionality‐multiplexing capability in metasurface design based on statistical machine learning. *Adv Mater* **34**, 2110022 (2022).
54. Ma W, Cheng F, Xu YH, Wen QL, Liu YM. Probabilistic representation and inverse design of metamaterials based on a deep generative model with semi‐supervised learning strategy. *Adv Mater* **31**, 1901111 (2019).
55. So S, Rho J. Designing nanophotonic structures using conditional deep convolutional generative adversarial networks. *Nanophotonics* **8**, 1255–1261 (2019).
56. Liu ZC, Zhu DY, Lee KT, Kim AS, Raju L et al. Compounding meta‐atoms into metamolecules with hybrid artificial intelligence techniques. *Adv Mater* **32**, 1904790 (2020).
57. Kudyshev ZA, Kildishev AV, Shalaev VM, Boltasseva A. Machine-learning-assisted metasurface design for high-efficiency thermal emitter optimization. *Appl Phys Rev* **7**, 021407 (2020).
58. Lin X, Rivenson Y, Yardimci NT, Veli M, Luo Y et al. All-optical machine learning using diffractive deep neural networks. *Science* **361**, 1004–1008 (2018).
59. Zhu DY, Liu ZC, Raju L, Kim AS, Cai WS. Building multifunctional metasystems *via* algorithmic construction. *ACS Nano* **15**, 2318–2326 (2021).
60. Phan T, Sell D, Wang EW, Doshay S, Edee K et al. High-efficiency, large-area, topology-optimized metasurfaces. *Light Sci Appl* **8**, 48 (2019).
61. Pestourie R, Pérez-Arancibia C, Lin Z, Shin W, Capasso F et al. Inverse design of large-area metasurfaces. *Opt Express* **26**, 33732–33747 (2018).

62. Arbabi A, Horie Y, Ball AJ, Bagheri M, Faraon A. Subwavelength-thick lenses with high numerical apertures and large efficiency based on high-contrast transmitarrays. *Nat Commun* **6**, 7069 (2015).
63. Pu MB, Guo YH, Li X, Ma XL, Luo XG. Revisitation of extraordinary young's interference: from catenary optical fields to spin–orbit interaction in metasurfaces. *ACS Photonics* **5**, 3198–3204 (2018).
64. Luo XG, Pu MB, Guo YH, Li X, Zhang F et al. Catenary functions meet electromagnetic waves: opportunities and promises. *Adv Opt Mater* **8**, 2001194 (2020).
65. Pu MB, Li X, Ma XL, Wang YQ, Zhao ZY et al. Catenary optics for achromatic generation of perfect optical angular momentum. *Sci Adv* **1**, e1500396 (2015).
66. Aiazzi B, Alparone L, Baronti S, Selva M, Stefani L. Unsupervised estimation of signal-dependent CCD camera noise. *EURASIP J Adv Signal Process* **2012**, 231 (2012).

Acknowledgements

This work was supported by the National Key Research and Development Program (2021YFA1401000), the National Natural Science Foundation of China (No. 61975210, 62175242 and 62305345), Sichuan Science and Technology Program (2020YFJ0001).

Author contributions

M. B. Pu, Y. L. Ha and Y. Luo proposed the idea, Y. L. Ha and Y. Luo carried out the simulations and prepared the manuscript. Q. He fabricated the metasurfaces. Y. Luo, F. Zhang and J. J. Jin measured the optical properties of the metasurfaces. M. B. Pu and X. G. Luo supervised the project. All the authors analyzed the data and discussed the results. The authors read and approved the final manuscript.

Competing interests

The authors declare no competing financial interests.

Supplementary information

Supplementary information for this paper is available at https://doi.org/10.29026/oea.2023.230133